iScience

CellPress
OPEN ACCESS

Article

Prevention and regression of megamitochondria and steatosis by blocking mitochondrial fusion in the liver

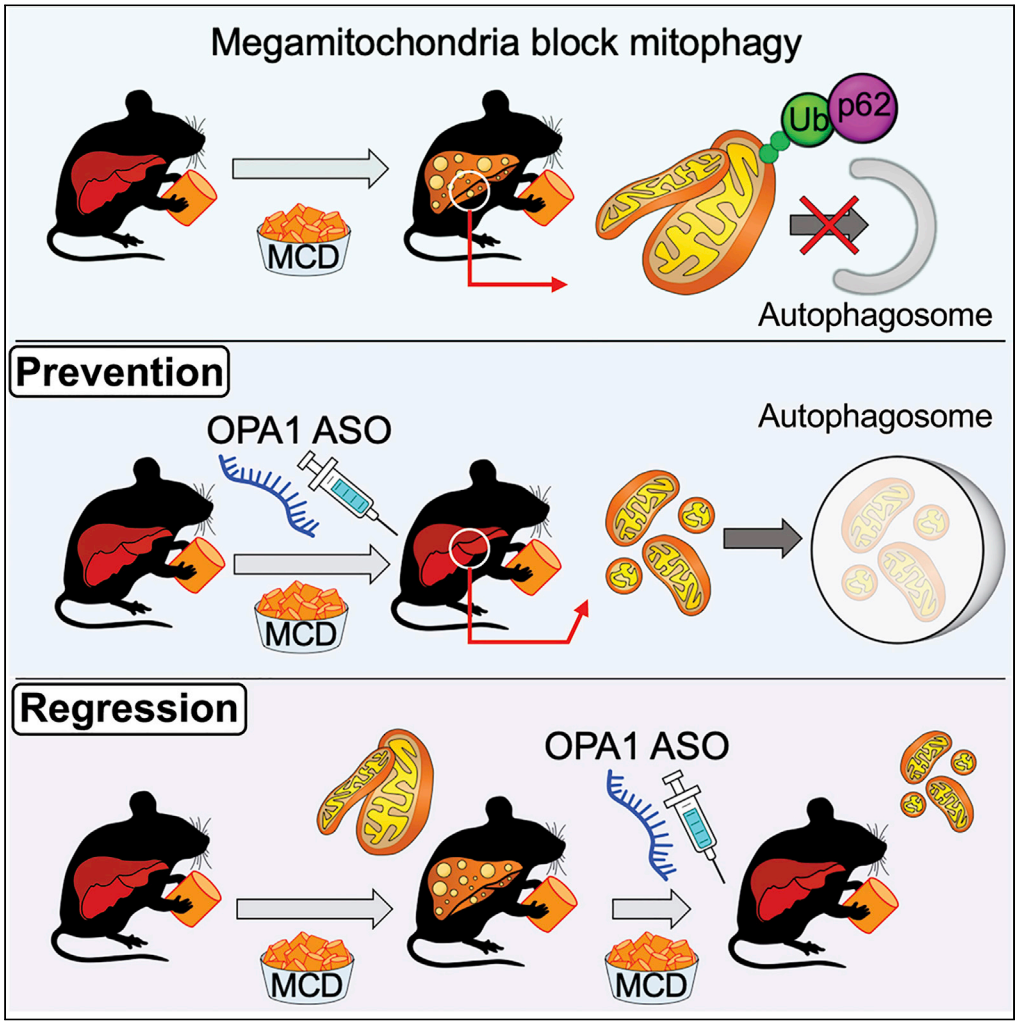

Tatsuya Yamada, Daisuke Murata, David E. Kleiner, ..., Andrew F. Powers, Miho Iijima, Hiromi Sesaki

miijima@jhmi.edu (M.I.)
hsesaki@jhmi.edu (H.S.)

Highlights

A NASH mouse model induced by the MCD diet produces megamitochondria in hepatocytes

Megamitochondria decrease mitophagy

Blocking mitochondrial fusion by targeting OPA1 mitigates NASH pathologies

Targeting OPA1 improves the SDH activity in the MCD model

Yamada et al., iScience *25*, 103996
April 15, 2022
https://doi.org/10.1016/j.isci.2022.103996

iScience

CellPress
OPEN ACCESS

Article

Prevention and regression of megamitochondria and steatosis by blocking mitochondrial fusion in the liver

Tatsuya Yamada,[1] Daisuke Murata,[1] David E. Kleiner,[2] Robert Anders,[3] Avi Z. Rosenberg,[3] Jeffrey Kaplan,[4] James P. Hamilton,[5] Mariam Aghajan,[6] Moshe Levi,[7] Nae-Yuh Wang,[8,9] Ted M. Dawson,[10,11] Toru Yanagawa,[12] Andrew F. Powers,[6] Miho Iijima,[1,*] and Hiromi Sesaki[1,13,*]

[1]Department of Cell Biology, Johns Hopkins University School of Medicine, Baltimore, MD, USA

[2]Laboratory of Pathology, National Cancer Institute, Bethesda, MD, USA

[3]Department of Pathology, Johns Hopkins University School of Medicine, Baltimore, MD, USA

[4]Department of Pathology, University of Colorado School of Medicine, Aurora, CO, USA

[5]Department of Medicine, Johns Hopkins University School of Medicine, Baltimore, MD, USA

[6]Ionis Pharmaceuticals, Carlsbad, CA, USA

[7]Department of Biochemistry and Molecular & Cellular Biology, Georgetown University, Washington, DC, USA

[8]Department of Medicine, Johns Hopkins University School of Medicine, Baltimore, MD, USA

[9]Department of Biostatistics, Johns Hopkins University Bloomberg School of Public Health, Baltimore, MD, USA

[10]Departments of Neurology and Neuroscience and Pharmacology and Molecular Sciences, Johns Hopkins University School of Medicine, Baltimore, MD, USA

[11]Neuroregeneration and Stem Cell Programs, Institute for Cell Engineering, Johns Hopkins University School of Medicine, Baltimore, MD, USA

[12]Department of Oral and Maxillofacial Surgery, Faculty of Medicine, University of Tsukuba, Ibaraki, Japan

[13]Lead contact

*Correspondence: miijima@jhmi.edu (M.I.), hsesaki@jhmi.edu (H.S.)

https://doi.org/10.1016/j.isci.2022.103996

SUMMARY

Non-alcoholic steatohepatitis (NASH) is a most common chronic liver disease that is manifested by steatosis, inflammation, fibrosis, and tissue damage. Hepatocytes produce giant mitochondria termed megamitochondria in patients with NASH. It has been shown that gene knockout of OPA1, a mitochondrial dynamin-related GTPase that mediates mitochondrial fusion, prevents megamitochondria formation and liver damage in a NASH mouse model induced by a methionine-choline-deficient (MCD) diet. However, it is unknown whether blocking mitochondrial fusion mitigates NASH pathologies. Here, we acutely depleted OPA1 using antisense oligonucleotides in the NASH mouse model before or after megamitochondria formation. When OPA1 ASOs were applied at the disease onset, they effectively prevented megamitochondria formation and liver pathologies in the MCD model. Notably, even when applied after mice robustly developed NASH pathologies, OPA1 targeting effectively regressed megamitochondria and the disease phenotypes. Thus, our data show the efficacy of mitochondrial dynamics as a unique therapy for megamitochondria-associated liver disease.

INTRODUCTION

Non-alcoholic steatohepatitis (NASH) is a severe form of non-alcoholic fatty liver disease that is manifested by hepatic steatosis, lobular inflammation, and fibrosis (Targher et al., 2018; Vreman et al., 2017; Younossi et al., 2019). This disease presents a widespread and rapidly growing problem and imparts huge economic and clinical burdens on society, for example, with up to 30 million people being affected in the United States alone (Targher et al., 2018; Vreman et al., 2017; Younossi et al., 2019). By 2030, its prevalence is estimated to increase by more than 50% (Estes et al., 2018). As the disease progress, up to 20% of patients with NASH develop cirrhosis, and 10% die due to liver failure or cancer (Ahmed et al., 2015; Calzadilla Bertot and Adams, 2016). It is unknown how fatty liver diseases develop into severe NASH. Although NASH is often associated with obesity and diabetes, it can be manifested in lean individuals who are not overweight or show insulin resistance. Currently, no medications are approved to treat NASH. Therefore, an urgent need to understand the mechanisms of the disease and to develop a treatment strategy exists (Ahmed et al., 2015; Alkhouri and Feldstein, 2016; Schuster et al., 2018).

Defects in mitochondrial structure and function have been linked to NASH. Hepatocytes in patients with NASH contain extremely enlarged mitochondria called megamitochondria (Kleiner, 2018; Lee et al., 2019; Roy et al., 2015; Takahashi and Fukusato, 2014). It has been shown that megamitochondria are resistant to engulfment by autophagosomes and can escape mitophagy, a selective autophagic degradation process for eliminating damaged mitochondria (Kageyama et al., 2014; Yamada et al., 2018). Decreased mitophagy slows the removal of damaged mitochondria, leads to the accumulation of oxidative damage, and compromises mitochondrial respiration function (Lee et al., 2019; Roy et al., 2015).

In the current study, to investigate the effect of targeting megamitochondria as a treatment for NASH, we screened multiple diet-induced mouse NASH models. We found that the MCD diet most effectively produced megamitochondria similar to human patients with NASH.

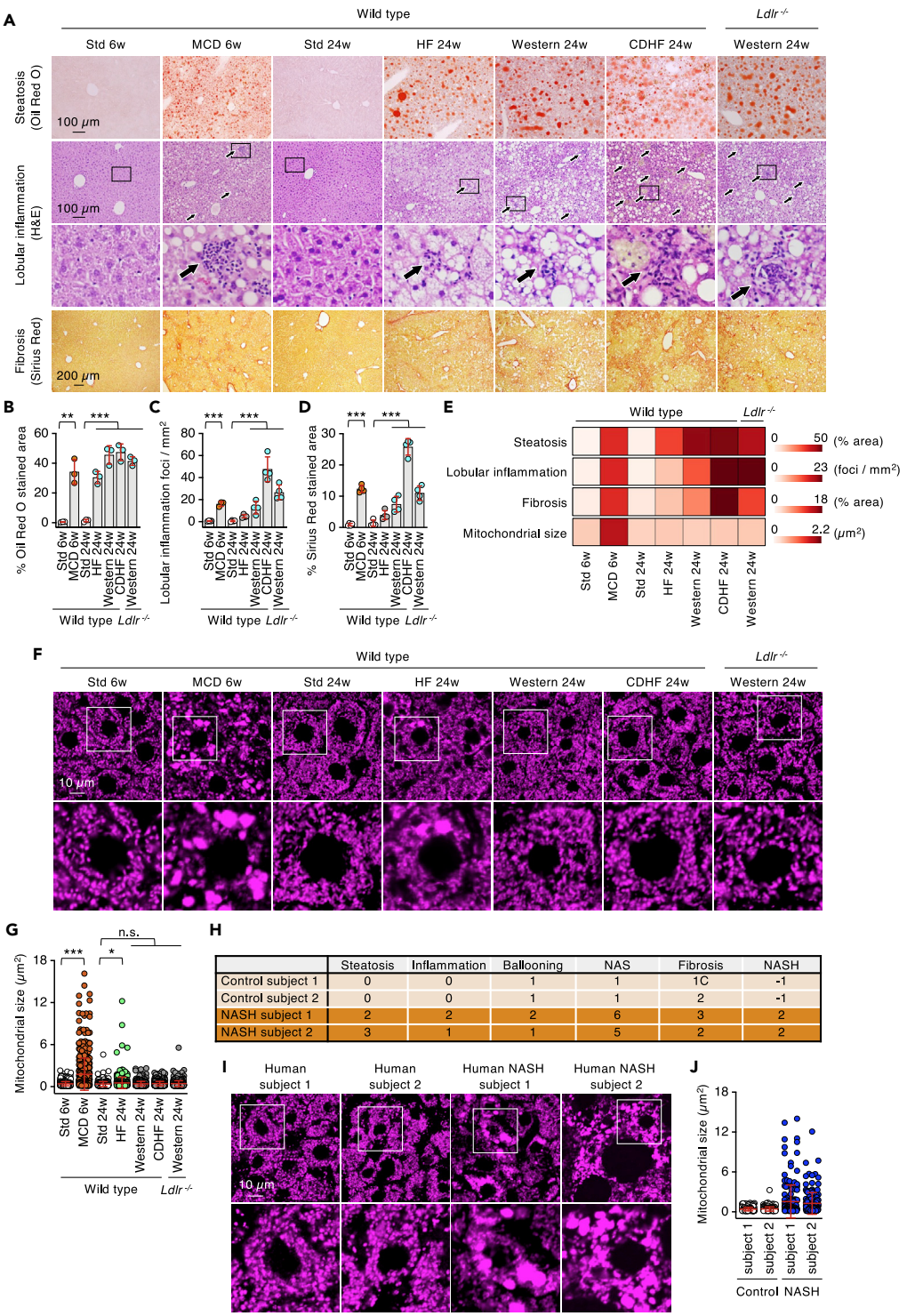

	Steatosis	Inflammation	Ballooning	NAS	Fibrosis	NASH
Control subject 1	0	0	1	1	1C	-1
Control subject 2	0	0	1	1	2	-1
NASH subject 1	2	2	2	6	3	2
NASH subject 2	3	1	1	5	2	2

Figure 1. Megamitochondria are formed in mouse MCD diet model and human patients with NASH

(A) Liver sections from the indicated NASH mouse models were analyzed by Oil Red O staining for steatosis, H&E (H&E) staining for lobular inflammation, and Sirius Red staining for fibrosis. Boxed regions are enlarged.

(B–D) Quantification of steatosis in (B), lobular inflammation in (C), and fibrosis in (D) are shown. Bars are average ± SD (n = three to four mice).

(E) Heatmap summary of histopathology and mitochondrial size.

Figure 1. *Continued*

(F) Cryosections of livers from the indicated NASH mouse models were subjected to laser confocal immunofluorescence microscopy using antibodies to a mitochondrial protein, pyruvate dehydrogenase (PDH). Boxed regions are enlarged.

(G) Quantification of mitochondrial size. Bars are average ± SD for n = 500–600 mitochondria for each experimental group.

(H) Histological scoring of liver sections from human patients using the NASH Clinical Research Network scoring system (Kleiner et al., 2005).

(I) Mitochondria were visualized by immunofluorescence microscopy with anti-PDH antibodies in the same set of human patients with NASH described in (H). Boxed regions are enlarged.

(J) Quantification of mitochondrial size. Bars are average ± SD (n = 203 for control subject 1, 215 for control subject 2, 178 for NASH subject 1, 170 for NASH subject 2). Statistical analysis was performed using Student's *t* test in (B, C, D, and G; Std 6w and MCD 6w) and one-way ANOVA with post-hoc Dunnett's test in (B, C, D, and G; Std 24w and other diets 24w): *$p < 0.05$, **$p < 0.01$, ***$p < 0.001$.

Using this preclinical model, we tested whether acute knockdown of OPA1, a dynamin-related GTPase mediating mitochondrial fusion, can regress megamitochondria and liver pathology after strong disease manifestation.

RESULTS

Identification of mouse NASH models that produce megamitochondria

To identify NASH mouse models that produce megamitochondria in hepatocytes, we systematically examined five major dietary-induced preclinical mouse models for NASH (Farrell et al., 2018; Van Herck et al., 2017). In four models, wild-type C57BL/6J mice (WT mice) were fed with four different types of NASH-inducing diets. These dietary treatments include a methionine- and choline-deficient diet (MCD model) for six weeks (Farrell et al., 2018; Van Herck et al., 2017), high-fat diet (HF model) for 24 weeks (Farrell et al., 2018; Van Herck et al., 2017), Western diet (Western model) for 24 weeks (Farrell et al., 2018; Van Herck et al., 2017), and choline-deficient high-fat diet (CDHF model) for 24 weeks (Abe et al., 2019) as shown in Figure 1A. We also fed mice lacking low-density lipoprotein receptor (Ldlr-KO mice) with the Western diet for 24 weeks (Ldlr-KO-Western model), which displays increased liver inflammation (Bieghs et al., 2012). HF and Western diets increase body weight and insulin resistance, similar to human patients with NASH with obesity and diabetes, while MCD and CDHF do not cause an increase in body weight, similar to NASH in lean individuals (Farrell et al., 2018; Van Herck et al., 2017). At the end of the dietary treatments, mice were subjected to cardiac perfusion with paraformaldehyde. Livers were then dissected and analyzed for the hallmarks of NASH histopathology, including steatosis, lobular inflammation, and fibrosis.

We found that all of the five dietary NASH models show robust steatosis revealed by Oil Red O staining (Figures 1A, 1B, and 1E). The highest increases in lobular inflammation were found in the CDHF and Ldlr-KO-Western models (Figures 1A, 1C, and 1E). Relatively modest lobular inflammation was observed in MCD and Western models (Figures 1A, 1C, and 1E). Fibrosis is an aberrant accumulation of extracellular matrix components, such as collagen, and results from inflammation and/or tissue damage (Sheka et al., 2020). Sirius Red staining that labels collagen showed that fibrosis was increased to different levels in all five models with the highest level in CDHF model (Figures 1A, 1D, and 1E).

Laser confocal immunofluorescence microscopy with antibodies to a mitochondrial protein, pyruvate dehydrogenase (PDH), revealed megamitochondria formation in MCD and HF models (Figures 1E–1G) (Yamada et al., 2018). Compared to the MCD model, the frequency of megamitochondria formed in the HF model was relatively modest (Figures 1E–1G). In contrast, the other three models did not show significant increases in mitochondrial size. The size of megamitochondria found in the mouse MCD and HF model was similar to that in human patients with NASH (Figures 1H–1J). Thus, while all of the five dietary NASH mouse models developed marked steatosis in the liver, other NASH pathologies, lobular inflammation, fibrosis, and megamitochondria, were manifested to different degrees. These data are consistent with the notion that NASH is a multifactorial, heterogeneous liver disease and steatosis is not a solo cause of liver pathologies.

Targeting OPA1 prevents steatosis, inflammation, fibrosis, and liver injury in megamitochondria-associated NASH

Mitochondrial size is controlled by a balance between mitochondrial fusion and division. We have previously shown that mice that lost the mitochondrial fusion GTPase OPA1 in the liver are resistant to the formation of MCD diet-induced megamitochondria (Yamada et al., 2018). These data suggest that megamitochondria

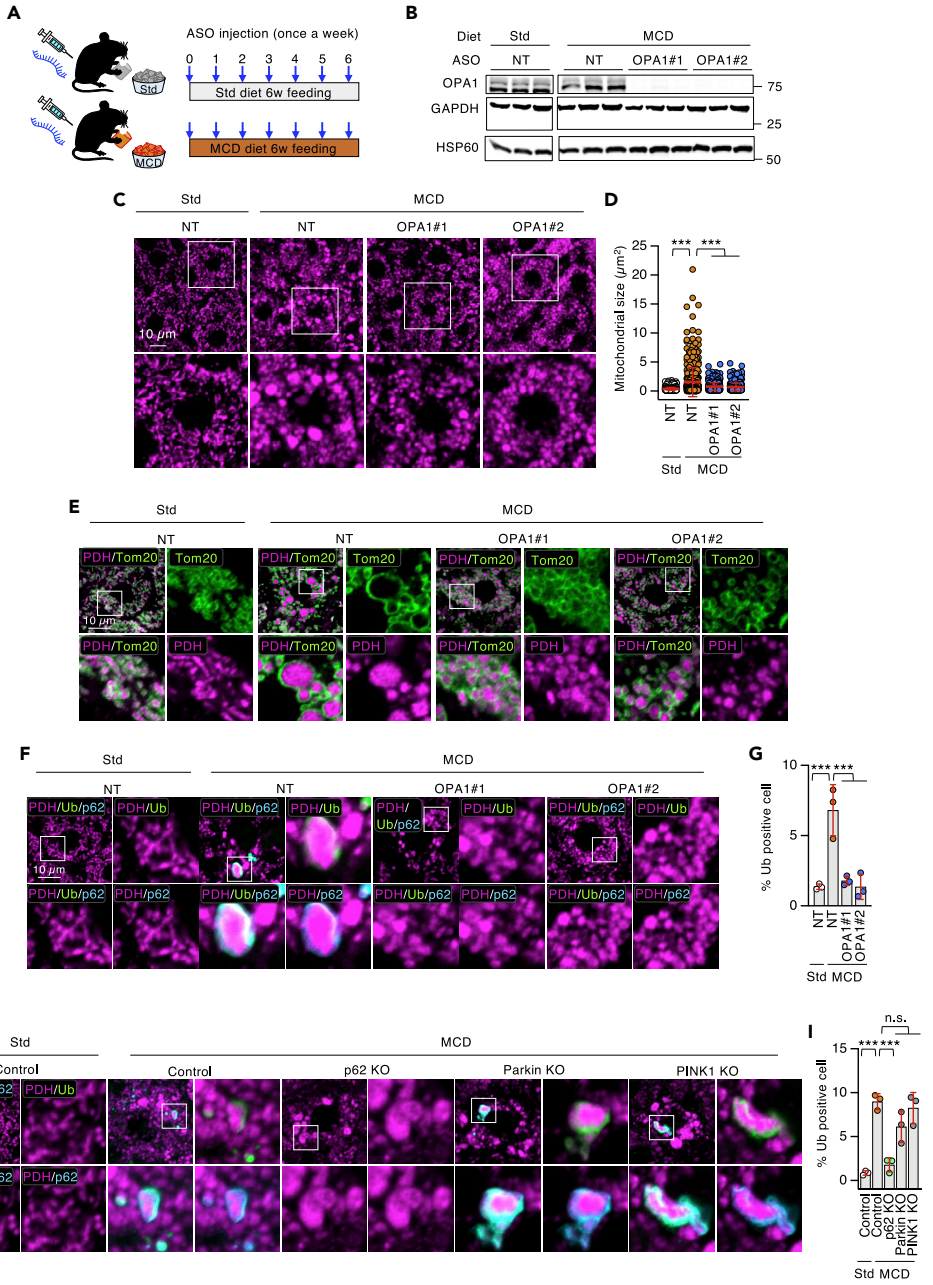

Figure 2. OPA1 ASOs block megamitochondria formation

(A) Experimental design. Mice were fed with an MCD or standard diet for six weeks. Non-targeting control ASOs (NT) or two independent OPA1-targeted ASOs (50 mg/kg bodyweight) were intraperitoneally injected into mice once a week for 6 weeks.

(B) Western blotting of livers using antibodies to OPA1, GAPDH, and a mitochondrial protein, HSP60. Three mice were analyzed for each experimental condition.

(C–E) Liver cryosections were analyzed by laser confocal immunofluorescence microscopy with antibodies to PDH (C and D) and PDH and TOM20 (E). Boxed regions are enlarged. (D) Individual mitochondrial sizes were analyzed. Bars are average ± SD (n = 400–500 mitochondria for each experimental group).

(F) Liver cryosections were subjected to immunofluorescence microscopy with antibodies to PDH (magenta), ubiquitin (green), and p62 (blue). Boxed regions are enlarged.

(G) Cells that show ubiquitin accumulation are quantified. Bars are average ± SD (n = 3 mice).

Figure 2. *Continued*

(H) Liver sections from the indicated mouse lines were analyzed by immunofluorescence microscopy with antibodies to PDH, ubiquitin, and p62. Boxed regions are enlarged.

(I) Cells with ubiquitin accumulation are quantified. Bars are average ± SD (n = 3 mice). Statistical analysis was performed using one-way ANOVA with post-hoc Dunnett's test in (D, G, and I; MCD + NT and other groups): ***p < 0.001.

formation can be blocked when OPA1 is inactivated prior to the induction of NASH. However, in this study, OPA1 was lost during embryonic development by hepatocyte-specific albumin-Cre recombinase (Postic et al., 1999), and this timing is much earlier than that of NASH induction at six weeks of age.

To acutely and reversibly inhibit OPA1 during NASH pathogenesis, we knocked down OPA1 using ASOs in the MCD model (Figure 2A). ASOs are short, single-stranded oligonucleotides that bind to mRNA targets and induce RNase H1-mediated degradation of target mRNAs (Crooke et al., 2019; Rinaldi and Wood, 2018; Shen and Corey, 2018). We intraperitoneally injected two distinct OPA1-targeted ASOs into mice once a week during the 6-week induction of NASH (Figure 2A). Western blotting of livers showed a great decrease in OPA1 levels by both OPA1-targeted ASOs compared to a non-targeted control ASO in MCD model (Figure 2B). Laser confocal immunofluorescence microscopy studies with anti-PDH antibodies revealed that OPA1 ASOs, but not the non-targeted control ASOs, caused a decrease in the size of mitochondria in the MCD model (Figures 2C and 2D). We further confirmed the changes in mitochondrial morphology by double immunostaining of the outer membrane TOM20 and the matrix protein PDH (Figure 2E). The TOM20 staining surrounded the PDH staining.

In addition, megamitochondria accumulate ubiquitin and p62, which functions both upstream and downstream of ubiquitination, in the MCD model due to mitochondrial damage (Yamada et al., 2018, 2019) (Figures 2F and 2G). Importantly, OPA1 ASOs effectively decreased the accumulation of ubiquitination and p62 (Figures 2F and 2G). Furthermore, we found that the ubiquitination was much lost in the absence of p62, but not ubiquitin E3 ligase, Parkin, or its activator kinase, PINK1, in the MCD model (Figures 2H and 2I).

We found that the critical NASH pathologies are prevented by OPA1 ASOs. Oil Red O staining revealed that steatosis was greatly decreased by OPA1 ASOs, but not control ASOs (Figures 3A, 3B, and 3F). Lobular inflammation and fibrosis were also significantly, but to lesser extents compared to steatosis, prevented by OPA1 ASOs (Figures 3A, 3C, 3D, and 3F). Consistent with the decrease in fibrosis, real-time qPCR showed decreases in mRNA levels of collagen A1 (Figure 4C and Table S1). Hepatocellular injury was decreased following treatment with OPA1-targeted ASOs as evidenced by a decrease in serum levels of alanine aminotransferase (ALT), which is released from hepatocytes as a consequence of liver injury (Figures 3E and 3F). The MCD diet decreased body weight and liver size (Figures 3G and 3H), consistent with previous studies (Farrell et al., 2018; Van Herck et al., 2017). We found that OPA1 ASOs do not affect body weight and liver size in the MCD model (Figures 3G and 3H); therefore, the mitigation effects of OPA1 ASOs on liver pathology are independent of body weight and liver size. Taken together, these data show that OPA1 ASOs effectively prevent the pathogenesis of NASH in the MCD model.

Because the MCD diet has been shown to decrease triglyceride secretion, serum levels of lipids were measured to understand how OPA1 ASOs cause a decrease in steatosis (Rinella et al., 2008). Consistent with the previous study, serum triglyceride and cholesterol levels were reduced in the MCD model; however, OPA1 ASOs did not rescue triglyceride and cholesterol levels (Figures 4A and 4B). Although we did not directly measure lipid secretion, it is possible that OPA1 ASOs do not promote the release of these lipids into the blood from the liver.

Second, we analyzed mRNA levels for genes that are involved in lipid synthesis, lipoprotein transport, fatty acid uptake, and peroxisomal and mitochondrial β-oxidation (Table S1 and Figure 4C). We observed increases in several genes such as acetyl-CoA carboxylase 1 (ACC1), glycerol-3-phosphate acyltransferase 1 (GPAT1), acyl-CoA thioesterases 2 (ACOT2), and fatty acid translocase (CD36) in the MCD model. Expression levels of these genes were not decreased by OPA1 ASOs (Figure 4C and Table S1). These data suggest that lipid synthesis is increased in the MCD model, and that OPA1 ASOs minimally affect lipid synthesis at the level of gene expression. Third, we analyzed mitochondrial protein levels by Western blotting. We found that levels of the mitochondrial pyruvate carrier, MPC2, were decreased in the MCD model (Figures 4D, 4E, and 4F). Noticeably, OPA1 ASOs caused a substantial increase in its level in the MCD model (Figures 4D, 4E, and 4F). These data suggest that pyruvate import into the mitochondrial

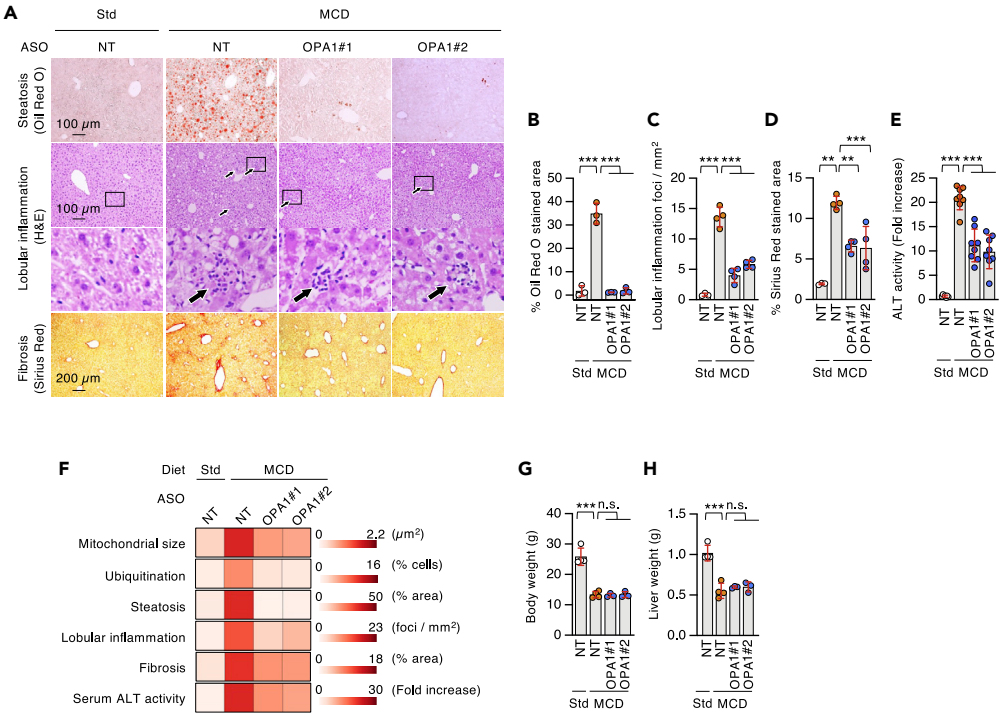

Figure 3. OPA1 ASOs prevent megamitochondria-associated NASH

(A–D) Histological analysis of livers. Quantification of steatosis (B), lobular inflammation (C), and fibrosis (D) are shown. Bars are average ± SD (n = three to four mice).

(E) Serum levels of ALT. ALT activity levels for each mouse were normalized to those for mice fed with standard diet and treated with non-targeting ASOs. Bars are average ± SD (n = seven to eight mice).

(F) Heatmap summary of the data.

(G and H) Body (G) and liver (H) weight of mice are shown. Bars are average ± SD (n = three to four mice). Statistical analysis was performed using one-way ANOVA with post-hoc Dunnett's test in (B, C, D, E, G, and H; MCD + NT and other groups): **p < 0.01, ***p < 0.001.

matrix across the inner membrane for the tricarboxylic acid (TCA) cycle decreased, but OPA1 ASOs could restore pyruvate import. Similar to MPC2, OPA1 ASOs had a positive impact on the succinate dehydrogenase (SDH) complex that consists of four subunits (SDHA–D). SDH functions in both the TCA cycle and oxidative phosphorylation as complex II in the electron transport chain. We found that protein levels of SDHA, B, and C were significantly decreased in the MCD model and restored in the presence of OPA1 ASOs (Figures 4D–4F). Notably, SDHC levels were further increased beyond the original level after treatment with OPA1 ASOs (Figures 4D–4F). These data suggest that OPA1 ASOs protect the integrity of TCA cycle and oxidative phosphorylation in the MCD model. It would be important to test whether these changes lead to mitochondrial catabolism of lipids or other metabolites in future studies.

How does mitochondrial size increase in the MCD model? Western blotting of livers showed that levels of the mechano-chemical GTPase dynamin-related protein 1 (DRP1) that mediates mitochondrial division and its major receptor, mitochondrial fission factor (MFF), did not decrease in the MCD model (Figures 4D and 4E). We have previously shown that saturated phospholipids inhibit the function of DRP1 (Adachi et al., 2016; Kameoka et al., 2018). Inhibition of stearoyl-CoA desaturase (SCD1) blocks mitochondrial division and enlarges mitochondria (Adachi et al., 2016; Kameoka et al., 2018). Our analysis for mRNA levels showed that the expression of the SCD1 gene is dramatically decreased in the MCD model, consistent with a previous study (Rizki et al., 2006), and was not rescued by OPA1-targeted ASOs (Figure 4C and Table S1). These data suggest that mitochondrial division is altered due to decreased DRP1 function regulated by lipids rather than DRP1 amounts.

Targeting OPA1 improves the SDH activity in megamitochondria-associated NASH

To directly examine the impact of OPA1 ASOs on mitochondrial function in the MCD model, we measured the activity of the electron transport chain complex II activity (SDH) and complex IV

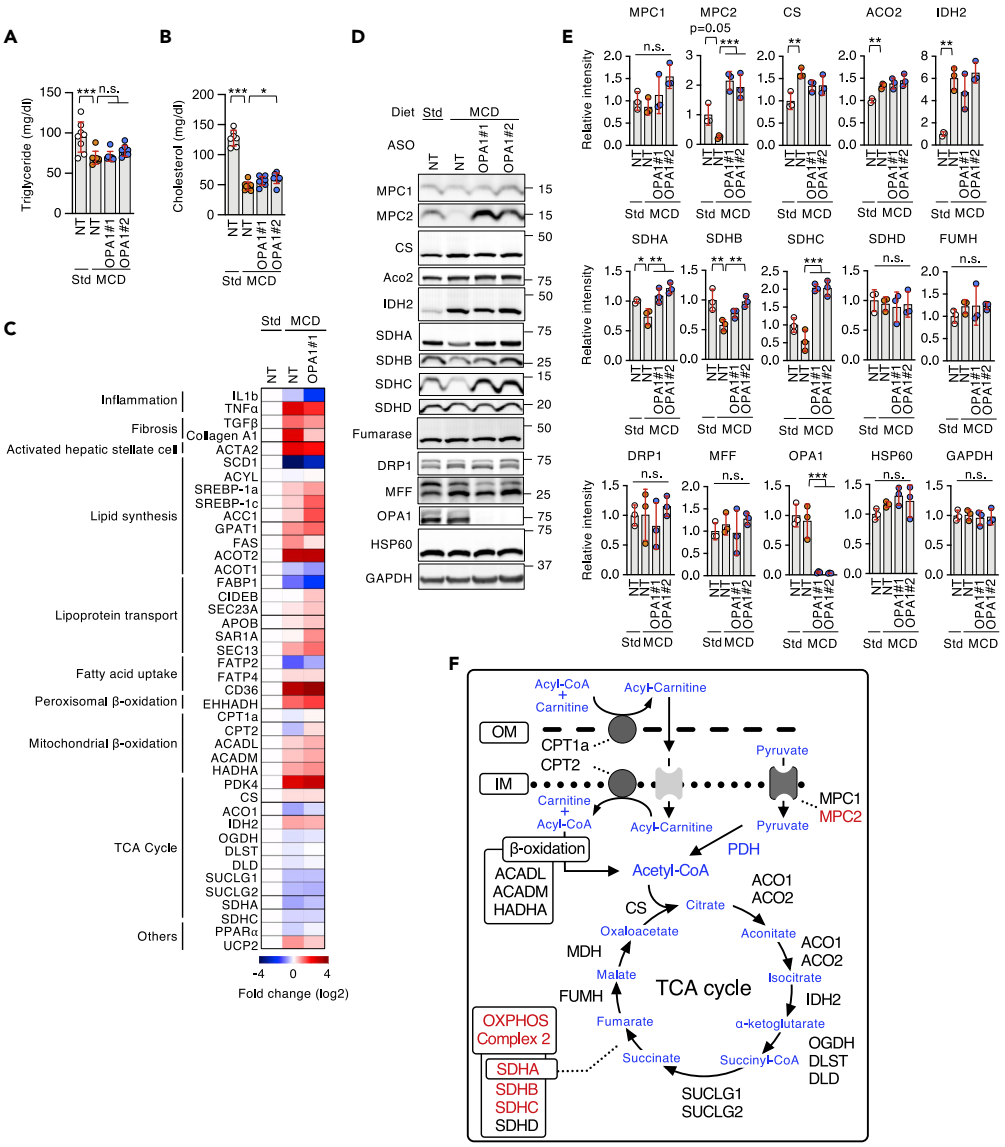

Figure 4. OPA1 ASOs increase levels of MPC2 and SDH subunits in megamitochondria-associated NASH

(A and B) Levels of serum triglyceride (A) and cholesterol (B). Bars are average ± SD (n = seven to eight mice).

(C) Heatmap summary of real-time qPCR analysis. Heatmap representing fold change of mRNA levels relative to those in mice that were fed with the standard diet and treated with non-targeting ASOs (Table S1).

(D) Western blotting of livers using the indicated antibodies was performed.

(E) Band intensity was quantified. Bars are average ± SD (n = 3 mice).

(F) Summary of the data. Protein levels of MPC2, SDHA, SDHB, and SDHC were lowered in the MCD model. OPA1 ASOs restored the level of MPC2, SDHA, and SDHB, and surpassed the original level of SDHC. Statistical analysis was performed using one-way ANOVA with post-hoc Dunnett's test in (A, B, and E; MCD + NT and other groups): *$p < 0.05$, **$p < 0.01$, ***$p < 0.001$.

(cytochrome *c* oxidase activity, COX) using histoenzymatic stains of unfixed, liver sections. We found that the SDH activity dramatically decreased in MCD model (Figures 5A and 5B). Both OPA1 ASOs restored the SDH activity to almost normal levels (Figures 5A and 5B). The increase is consistent with the increased levels of SDHA, B, and C (Figures 4D and 4E). In contrast, the COX activity showed a modest decrease in the MCD model, and OPA1 ASOs did not affect COX activity (Figures 5A and 5B).

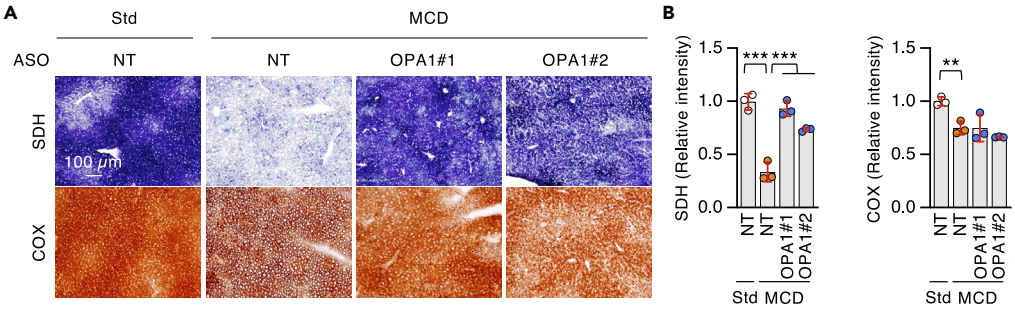

Figure 5. OPA1 ASOs maintain mitochondrial function in megamitochondria-associated NASH

(A) Fresh frozen sections of livers were enzymatically stained for activities of SDH and COX.

(B) Quantification of SDH and COX staining. Bars are average ± SD (n = 3). Statistical analysis was performed using one-way ANOVA with post-hoc Dunnett's test (MCD + NT and other groups): **p < 0.01, ***p < 0.001.

Targeting OPA1 regresses steatosis, inflammation, fibrosis, and liver injury in megamitochondria-associated NASH

The above data show that OPA1 ASOs can block megamitochondria formation and prevent NASH-related pathogenesis. We further sought to test whether targeting OPA1 can cause regression of NASH pathologies after the disease phenotypes have developed. To address this question, we first fed mice with the MCD diet for six weeks (Figure 6A). We then continued the MCD diet feeding for another six weeks with intraperitoneal injections of non-targeting or OPA1-targeted ASOs. Western blotting of livers showed that OPA1 was effectively knocked down by OPA1 ASOs (Figure 6B). OPA1 ASOs did not affect body weight or liver size (Figures 6C and 6D). In mice fed with the MCD diet for 12 weeks in conjunction with non-targeting ASOs, megamitochondria were formed and ubiquitinated as shown by laser confocal immunofluorescence microscopy with antibodies to PDH, ubiquitin, and p62 (Figures 6E–6H). In contrast, OPA1 ASOs significantly reversed mitochondrial size, ubiquitination, and p62 accumulation (Figures 6E–6H). Transmission electron microscopy showed that the inner membrane cristae appeared disorganized and were greatly lost in the MCD model (Figure 6I). Although mitochondrial size was rescued by OPA1 ASOs, the cristae remained disorganized (Figure 6I).

Oil Red O staining showed that steatosis was also dramatically reversed by OPA1 ASOs (Figures 6J, 6K, and 6P). Similarly, lobular inflammation and fibrosis were reversed by OPA1 ASOs (Figures 6J, 6L, 6M, and 6P). At the end of the 12 weeks of the MCD diet, hepatocyte ballooning was clearly observed (Figures 6J, 6N, and 6P). As with other histopathologic abnormalities, OPA1 ASOs effectively caused a decrease in hepatocyte ballooning although the rescue effect did not achieve a significant level (Figures 6J, 6N, and 6P). Finally, serum ALT levels were reduced by OPA1 ASOs in the MCD model (Figures 6O and 6P). Therefore, targeting OPA1 can cause reversal of mitochondrial size and NASH pathologies in the MCD model. Because the structural integrity of the cristae was not restored by OPA1 ASOs, their rescue effects were independent of the function of OPA1 in the cristae structure.

DISCUSSION

In this study, we showed that acute depletion of OPA1 induced by ASOs decreases mitochondrial size in a megamitochondria-associated NASH mouse model. Targeting OPA1 effectively prevented and regressed the major pathologies of NASH, including steatosis, inflammation, fibrosis, and liver damage. Because megamitochondria slow mitophagy of damaged mitochondria (Yamada et al., 2018), suppression of megamitochondria by blocking OPA1 might improve mitochondrial health and mitigate steatosis. For example, enhanced mitochondrial activities, such as the TCA cycle, oxidative phosphorylation, and fatty acid oxidation, might enable mitochondria to effectively readjust a balance between biosynthesis, transport, and breakdown of lipids.

In addition to mitochondrial fusion, OPA1 controls the morphogenesis of the inner mitochondrial membrane cristae, which provide a structural platform for COX. COX is a large protein complex that contains 14 main subunits with more than 10 accessory proteins. In MCD model, the activities of both SDH and COX decreased, and the cristae morphology was altered. OPA1 ASOs did not rescue cristae defects or COX activity in the MCD model. In contrast, the activity of SDH was rescued by OPA1 ASOs. SDH is a relatively simple complex with only four subunits. Because decreases in COX activity was modest

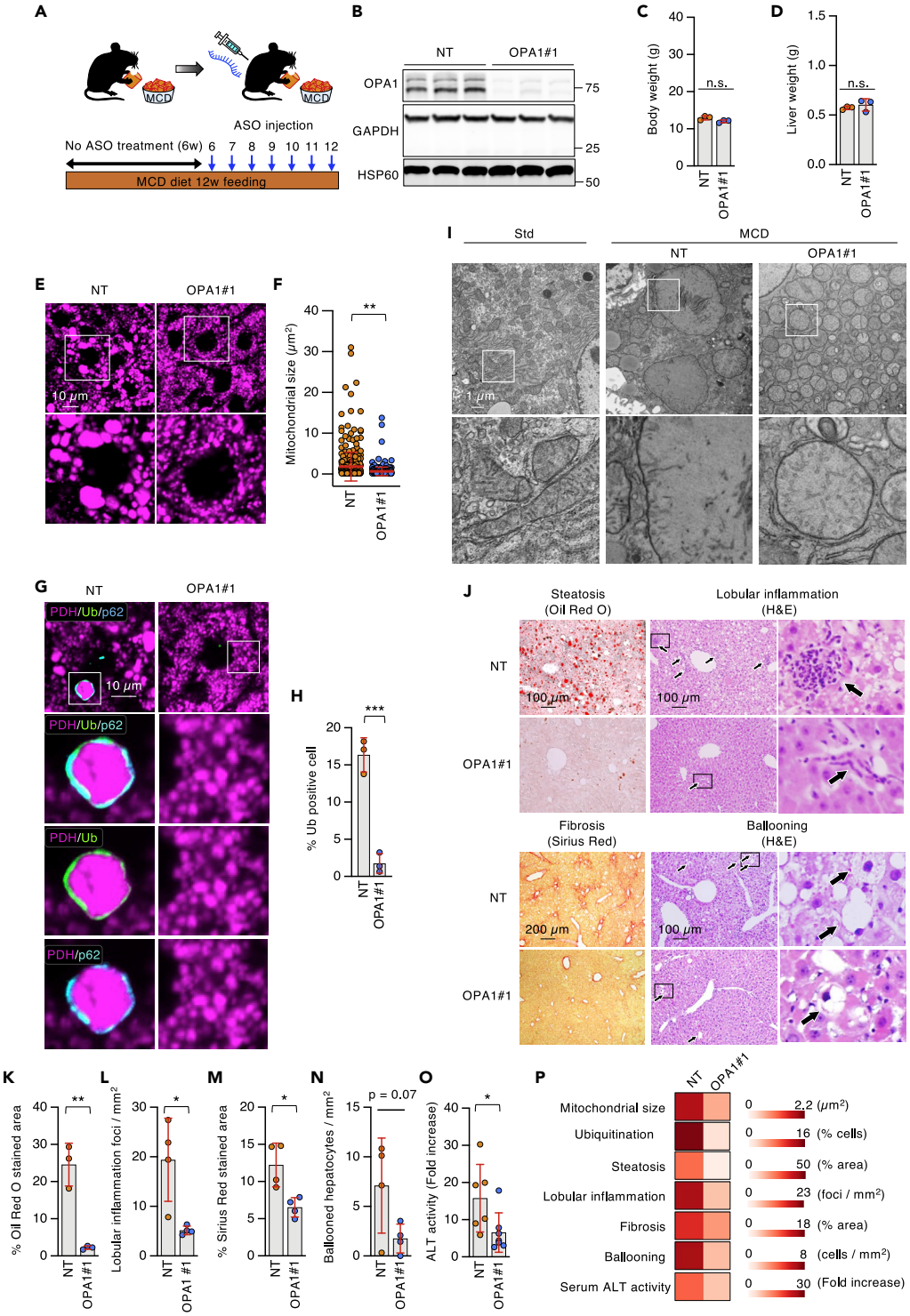

Figure 6. OPA1 ASOs regress megamitochondria-associated NASH

(A) Experimental design. Mice were first fed with MCD diet for 6 weeks without ASO treatment. Then, mice were continued to be fed with MCD diet with intraperitoneal injections of non-targeting (NT) or OPA1 ASOs once a week for 6 weeks.

(B) Western blotting of livers using antibodies to OPA1, GAPDH, and HSP60. Three mice were analyzed for each experimental condition.

(C and D) Body (C) and liver (D) weight of mice are shown. Bars are average ± SD (n = 3 mice).

Figure 6. *Continued*

(E) Liver cryosections were analyzed by laser confocal immunofluorescence microscopy with anti-PDH antibodies. Boxed regions are enlarged.

(F) Quantification of individual mitochondrial size. Bars are average ± SD (n = approximately 400 mitochondria for each experimental group).

(G) Liver cryosections were subjected to immunofluorescence microscopy with antibodies to PDH, ubiquitin, and p62. Boxed regions are enlarged.

(H) Cells that show ubiquitin accumulation are quantified. Bars are average ± SD (n = 3 mice).

(I) Transmission electron microscopy of livers in the indicated mice.

(J–N) Histological analysis of livers. Quantification of steatosis (K), lobular inflammation (L), fibrosis (M), and hepatocyte ballooning (N) are shown. Bars are average ± SD (n = three to four mice).

(O) Serum levels of ALT. ALT activity levels for each mouse were normalized to those for mice fed with standard diet and treated with non-targeting ASOs. Bars are average ± SD (n = six to seven mice).

(P) Heatmap summary of the data. Statistical analysis was performed using Student's *t* test in (C, D, F, H, and K–O): *p < 0.05, **p < 0.01, ***p < 0.001.

in the MCD model, a decrease in COX activity may be compensated for by an increase in SDH activity. We suggest that depleting OPA1 improves SDH but not COX, thereby, on balance, helping to maintain overall mitochondrial health in livers in the MCD model.

Working together with OPA1, two homologous dynamin-related GTPases, mitofusins 1 and 2, mediate mitochondrial fusion. While these two mitofusins could also be potential targets for treating megamitochondria-associated NASH, mitofusin 2 has an additional function in tethering the ER and mitochondria, which likely precludes mitofusin 2 as an effective drug target for liver diseases. For example, it has been reported that the liver-specific loss of mitofusin 2 inhibits the transport of phosphatidylserine from the ER to the mitochondria through their contact sites and results in NASH-like phenotypes and liver cancers (de Brito and Scorrano, 2008; Hernandez-Alvarez et al., 2019). In contrast, the liver-specific loss of mitofusin 1 causes a decrease in mitochondrial size and enhancement of mitochondrial respiration (Kulkarni et al., 2016). These data suggest that mitofusin 1, rather than mitofusin 2, would be a better therapeutic target, similar to OPA1, for megamitochondria-associated NASH.

Our systematic analyses of multiple mouse NASH models revealed that the MCD model most effectively produces megamitochondria out of the five major models tested in this study. In addition to megamitochondria, our side-by-side comparison of these NASH mouse models clearly showed different degrees of disease manifestation in different models. In humans, NASH is a complex metabolic disease and only a fraction of patients with non-alcoholic fatty liver becomes NASH (Targher et al., 2018; Vreman et al., 2017; Younossi et al., 2019). Although multiple factors such as genetics, environment, age, and lifestyle have been suggested to contribute to such differences, the exact underlying reason for NASH development is still unknown. The MCD model likely represents a subgroup of NASH, such as NASH in lean individuals, because the MCD model does not show obesity or metabolic aspects of human NASH, such as insulin tolerance. We envision that investigations of multiple NASH models with different pathogenetic mechanisms would enable a better understanding of multifaceted liver disease caused by critical changes in multiple metabolic and molecular pathways.

Limitations of the study

Our results clearly show that targeting OPA1 mitigates megamitochondria, steatosis, and histopathologies in the MCD model. However, further work is required to understand whether megamitochondria formation is the major cause of steatosis in the MCD model. While steatosis was almost entirely prevented by OPA1 ASOs, inflammation, fibrosis, and liver damage were still observed to some extent. Therefore, it appears that steatosis is not a solo driver of the histopathologies in the MCD model. In addition, other NASH models developed steatosis without robust megamitochondria formation, indicating that steatosis is not a simple consequence of mitochondrial enlargement. Finally, in future studies, it would be of great importance to elucidate how megamitochondria change mitochondrial bioenergetics and lipid metabolism through fatty acid oxidation, TCA cycle, and oxidative phosphorylation.

STAR★METHODS

Detailed methods are provided in the online version of this paper and include the following:

- KEY RESOURCES TABLE
- RESOURCE AVAILABILITY

SUPPLEMENTAL INFORMATION

Supplemental information can be found online at https://doi.org/10.1016/j.isci.2022.103996.

ACKNOWLEDGMENTS

We thank past and present members of the Iijima and Sesaki labs for helpful discussions and technical assistance. We are grateful to Dr. Alexander *M. van* der Bliek for the anti-MFF antibody. This work was supported by grants from NIH to MI (GM131768) and HS (GM130695 and GM144103), the Robert J. Kleberg, Jr. and Helen C. Kleberg Foundation to HS (Medical Research Grant), and the Hopkins Conte Digestive Diseases Basic and Translational Research Core Center to T. Yamada (Pilot/Feasibility Project).

AUTHOR CONTRIBUTIONS

T. Yamada, MI, and HS conceived the project. T. Yamada, DM, and DEK performed the experiments. T. Yamada, DM, DEK, and RA analyzed the data. MA, AZR, JK, ML, TMD, T. Yanagawa, and AFP provided critical materials and reagents. T. Yamada, DM, DEK, MA, AZR, JK, JPH, ML, NYW, TMD, T. Yanagawa, AFP, MI, and HS contributed to discussions. T. Yamada, JK, MI, and HS wrote the manuscript.

DECLARATION OF INTERESTS

T. Yamada, DM, DEK, RA, AZR, JK, JPH, ML, NYW, TMD, T. Yanagawa, MI, and HS declare that they have no competing interests. AFP and MA are employees and shareholders of Ionis Pharmaceuticals.

Received: November 3, 2021
Revised: January 6, 2022
Accepted: February 24, 2022
Published: April 15, 2022

REFERENCES

Abe, N., Kato, S., Tsuchida, T., Sugimoto, K., Saito, R., Verschuren, L., Kleemann, R., and Oka, K. (2019). Longitudinal characterization of diet-induced genetic murine models of non-alcoholic steatohepatitis with metabolic, histological, and transcriptomic hallmarks of human patients. Biol. Open *8*, bio041251.

Adachi, Y., Itoh, K., Yamada, T., Cerveny, K.L., Suzuki, T.L., Macdonald, P., Frohman, M.A., Ramachandran, R., Iijima, M., and Sesaki, H. (2016). Coincident phosphatidic acid interaction restrains Drp1 in mitochondrial division. Mol. Cell *63*, 1034–1043.

Ahmed, A., Wong, R.J., and Harrison, S.A. (2015). Nonalcoholic fatty liver disease review: diagnosis, treatment, and outcomes. Clin. Gastroenterol. Hepatol. *13*, 2062–2070.

Alkhouri, N., and Feldstein, A.E. (2016). Noninvasive diagnosis of nonalcoholic fatty liver disease: are we there yet? Metabolism *65*, 1087–1095.

Bieghs, V., Van Gorp, P.J., Wouters, K., Hendrikx, T., Gijbels, M.J., van Bilsen, M., Bakker, J., Binder, C.J., Lutjohann, D., Staels, B., et al. (2012). LDL receptor knock-out mice are a physiological model particularly vulnerable to study the onset of inflammation in non-alcoholic fatty liver disease. PLoS One *7*, e30668.

Calzadilla Bertot, L., and Adams, L.A. (2016). The natural course of non-alcoholic fatty liver disease. Int. J. Mol. Sci. *17*, 774.

Cioffi, C.L., Garay, M., Johnston, J.F., McGraw, K., Boggs, R.T., Hreniuk, D., and Monia, B.P. (1997). Selective inhibition of A-Raf and C-Raf mRNA expression by antisense oligodeoxynucleotides in rat vascular smooth muscle cells: role of A-Raf

and C-Raf in serum-induced proliferation. Mol. Pharmacol. *51*, 383–389.

Crooke, S.T., Witztum, J.L., Bennett, C.F., and Baker, B.F. (2019). RNA-targeted therapeutics. Cell Metab. *29*, 501.

de Brito, O.M., and Scorrano, L. (2008). Mitofusin 2 tethers endoplasmic reticulum to mitochondria. Nature *456*, 605–610.

Estes, C., Razavi, H., Loomba, R., Younossi, Z., and Sanyal, A.J. (2018). Modeling the epidemic of nonalcoholic fatty liver disease demonstrates an exponential increase in burden of disease. Hepatology *67*, 123–133.

Farrell, G., Schattenberg, J.M., Leclercq, I., Yeh, M.M., Goldin, R., Teoh, N., and Schuppan, D. (2018). Mouse models of nonalcoholic steatohepatitis towards optimization of their relevance to human NASH. Hepatology *69*, 2241–2257.

Gandre-Babbe, S., and van der Bliek, A.M. (2008). The novel tail-anchored membrane protein Mff controls mitochondrial and peroxisomal fission in mammalian cells. Mol. Biol. Cell *19*, 2402–2412.

Hernandez-Alvarez, M.I., Sebastian, D., Vives, S., Ivanova, S., Bartoccioni, P., Kakimoto, P., Plana, N., Veiga, S.R., Hernandez, V., Vasconcelos, N., et al. (2019). Deficient endoplasmic reticulum-mitochondrial phosphatidylserine transfer causes liver disease. Cell *177*, 881–895.e17.

Kageyama, Y., Hoshijima, M., Seo, K., Bedja, D., Sysa-Shah, P., Andrabi, S.A., Chen, W., Hoke, A., Dawson, V.L., Dawson, T.M., et al. (2014). Parkin-independent mitophagy requires Drp1 and maintains the integrity of mammalian heart and brain. EMBO J. *33*, 2798–2813.

Kageyama, Y., Zhang, Z., Roda, R., Fukaya, M., Wakabayashi, J., Wakabayashi, N., Kensler, T.W., Reddy, P.H., Iijima, M., and Sesaki, H. (2012). Mitochondrial division ensures the survival of postmitotic neurons by suppressing oxidative damage. J. Cel. Biol. *197*, 535–551.

Kameoka, S., Adachi, Y., Okamoto, K., Iijima, M., and Sesaki, H. (2018). Phosphatidic acid and cardiolipin coordinate mitochondrial dynamics. Trends Cell Biol *28*, 67–76.

Kleiner, D.E. (2018). Histopathology, grading and staging of nonalcoholic fatty liver disease. Minerva Gastroenterol. Dietol. *64*, 28–38.

Kleiner, D.E., Brunt, E.M., Van Natta, M., Behling, C., Contos, M.J., Cummings, O.W., Ferrell, L.D., Liu, Y.C., Torbenson, M.S., Unalp-Arida, A., et al. (2005). Design and validation of a histological scoring system for nonalcoholic fatty liver disease. Hepatology *41*, 1313–1321.

Kulkarni, S.S., Joffraud, M., Boutant, M., Ratajczak, J., Gao, A.W., Maclachlan, C., Hernandez-Alvarez, M.I., Raymond, F., Metairon, S., Descombes, P., et al. (2016). Mfn1 deficiency in the liver protects against diet-induced insulin resistance and enhances the hypoglycemic effect of metformin. Diabetes *65*, 3552–3560.

Lee, J., Park, J.S., and Roh, Y.S. (2019). Molecular insights into the role of mitochondria in non-alcoholic fatty liver disease. Arch. Pharm. Res. *42*, 935–946.

Postic, C., Shiota, M., Niswender, K.D., Jetton, T.L., Chen, Y., Moates, J.M., Shelton, K.D., Lindner, J., Cherrington, A.D., and Magnuson, M.A. (1999). Dual roles for glucokinase in glucose homeostasis as determined by liver and pancreatic beta cell-specific gene knock-outs using Cre recombinase. J. Biol. Chem. *274*, 305–315.

Rinaldi, C., and Wood, M.J.A. (2018). Antisense oligonucleotides: the next frontier for treatment of neurological disorders. Nat. Rev. Neurol. *14*, 9–21.

Rinella, M.E., Elias, M.S., Smolak, R.R., Fu, T., Borensztajn, J., and Green, R.M. (2008). Mechanisms of hepatic steatosis in mice fed a lipogenic methionine choline-deficient diet. J. Lipid Res. *49*, 1068–1076.

Rizki, G., Arnaboldi, L., Gabrielli, B., Yan, J., Lee, G.S., Ng, R.K., Turner, S.M., Badger, T.M., Pitas, R.E., and Maher, J.J. (2006). Mice fed a lipogenic methionine-choline-deficient diet develop hypermetabolism coincident with hepatic suppression of SCD-1. J. Lipid Res. *47*, 2280–2290.

Roy, M., Reddy, P.H., Iijima, M., and Sesaki, H. (2015). Mitochondrial division and fusion in metabolism. Curr. Opin. Cel. Biol. *33C*, 111–118.

Schuster, S., Cabrera, D., Arrese, M., and Feldstein, A.E. (2018). Triggering and resolution of inflammation in NASH. Nat. Rev. Gastroenterol. Hepatol. *15*, 349–364.

Seth, P.P., Vasquez, G., Allerson, C.A., Berdeja, A., Gaus, H., Kinberger, G.A., Prakash, T.P., Migawa, M.T., Bhat, B., and Swayze, E.E. (2010). Synthesis and biophysical evaluation of 2′,4′-constrained 2′O-methoxyethyl and 2′,4′-constrained 2′O-ethyl nucleic acid analogues. J. Org. Chem. *75*, 1569–1581.

Sheka, A.C., Adeyi, O., Thompson, J., Hameed, B., Crawford, P.A., and Ikramuddin, S. (2020). Nonalcoholic steatohepatitis: a review. JAMA *323*, 1175–1183.

Shen, X., and Corey, D.R. (2018). Chemistry, mechanism and clinical status of antisense oligonucleotides and duplex RNAs. Nucleic Acids Res. *46*, 1584–1600.

Takahashi, Y., and Fukusato, T. (2014). Histopathology of nonalcoholic fatty liver disease/nonalcoholic steatohepatitis. World J. Gastroenterol. *20*, 15539–15548.

Targher, G., Lonardo, A., and Byrne, C.D. (2018). Nonalcoholic fatty liver disease and chronic vascular complications of diabetes mellitus. Nat. Rev. Endocrinol. *14*, 99–114.

Van Herck, M.A., Vonghia, L., and Francque, S.M. (2017). Animal models of nonalcoholic fatty liver disease-A Starter's guide. Nutrients *9*, 1072.

Vickers, T.A., Koo, S., Bennett, C.F., Crooke, S.T., Dean, N.M., and Baker, B.F. (2003). Efficient reduction of target RNAs by small interfering RNA and RNase H-dependent antisense agents. a comparative analysis. J. Biol. Chem. *278*, 7108–7118.

Vreman, R.A., Goodell, A.J., Rodriguez, L.A., Porco, T.C., Lustig, R.H., and Kahn, J.G. (2017). Health and economic benefits of reducing sugar intake in the USA, including effects via non-alcoholic fatty liver disease: a microsimulation model. BMJ Open *7*, e013543.

Wakabayashi, N., Shin, S., Slocum, S.L., Agoston, E.S., Wakabayashi, J., Kwak, M.-K., Misra, V., Biswal, S., Yamamoto, M., and Kensler, T.W. (2010). Regulation of Notch1 Signaling by Nrf2: Implications for Tissue Regeneration. Sci. Signal. *3*, ra52. https://doi.org/10.1126/scisignal.2000762.

Wakabayashi, J., Zhang, Z., Wakabayashi, N., Tamura, Y., Fukaya, M., Kensler, T.W., Iijima, M., and Sesaki, H. (2009). The dynamin-related GTPase Drp1 is required for embryonic and brain development in mice. J. Cell Biol. *186*, 805–816.

Yamada, T., Dawson, T.M., Yanagawa, T., Iijima, M., and Sesaki, H. (2019). SQSTM1/p62 promotes mitochondrial ubiquitination independently of PINK1 and PRKN/parkin in Mitophagy. Autophagy *15*, 2012–2018.

Yamada, T., Murata, D., Adachi, Y., Itoh, K., Kameoka, S., Igarashi, A., Kato, T., Araki, Y., Huganir, R.L., Dawson, T.M., et al. (2018). Mitochondrial stasis reveals p62-Mediated ubiquitination in parkin-independent mitophagy and mitigates nonalcoholic fatty liver disease. Cell Metab. *28*, 588–604.

Younossi, Z.M., Tampi, R., Priyadarshini, M., Nader, F., Younossi, I.M., and Racila, A. (2019). Burden of illness and economic model for patients with nonalcoholic steatohepatitis in the United States. Hepatology *69*, 564–572.

Zhang, H., Cook, J., Nickel, J., Yu, R., Stecker, K., Myers, K., and Dean, N.M. (2000). Reduction of liver Fas expression by an antisense oligonucleotide protects mice from fulminant hepatitis. Nat. Biotechnol. *18*, 862–867.

STAR★METHODS

KEY RESOURCES TABLE

REAGENT or RESOURCE	SOURCE	IDENTIFIER
Antibodies		
Mouse monoclonal anti-Drp1	BD Biosciences	Cat# 611113; RRID: AB_398424
Mouse monoclonal anti-Opa1	BD Biosciences	Cat# 612607; RRID: AB_399889
Mouse monoclonal anti-PDH	abcam	Cat# ab110333; RRID: AB_10862029
Mouse monoclonal anti-GAPDH	Thermo Fisher Scientific	Cat# MA5-15738; RRID: AB_10977387
Rabbit monoclonal anti-HSP60	Cell Signaling Technology	Cat# 12165; RRID: AB_2636980
Guinea pig polyclonal anti-p62	Progen	Cat# GP62-C; RRID: AB_2687531
Rabbit polyclonal anti-TOM20	Proteintech	Cat# 11802-1-AP; RRID: AB_2207530
Rabbit polyclonal anti-ubiquitin	Cell Signaling Technology	Cat# 3933S; RRID: AB_2180538
Rabbit polyclonal anti-MPC1	Cell Signaling Technology	Cat# 14462; RRID: AB_2890191
Rabbit polyclonal anti-MPC2	Cell Signaling Technology	Cat# 46141; RRID: AB_2890191
Rabbit polyclonal anti-Citrate Synthase	Cell Signaling Technology	Cat# 14309; RRID: AB_2890191
Rabbit polyclonal anti-ACO2	Cell Signaling Technology	Cat# 6571; RRID: AB_2890191
Rabbit polyclonal anti-IDH2	Cell Signaling Technology	Cat# 56439; RRID: AB_2890191
Rabbit polyclonal anti-Fumarase	Cell Signaling Technology	Cat# 4567; RRID: AB_2890191
Rabbit polyclonal anti-SDHA	Cell Signaling Technology	Cat# 11998; RRID: AB_2890191
Mouse monoclonal anti-SDHB	Abcam	Cat# ab14714; RRID: AB_301432
Rabbit polyclonal anti-SDHC	Proteintech	Cat# 14575-1-AP; RRID: AB_2183291
Rabbit polyclonal anti-SDHD	ProSci	Cat# 6842; RRID: AB_2316024
Rabbit polyclonal anti-MFF	Gandre-Babbe and van der Bliek, 2008	N/A
Alexa 488 anti-rabbit IgG	Thermo Fisher Scientific	Cat# A-21206; RRID: AB_2535792
Alexa 488 anti-mouse IgG	Thermo Fisher Scientific	Cat# A-21202; RRID: AB_141607
Alexa 568 anti-mouse IgG	Thermo Fisher Scientific	Cat# A10037; RRID: AB_2534013
Alexa 647 anti-rabbit IgG	Thermo Fisher Scientific	Cat# A-31573; RRID: AB_2536183
Alexa 647 anti-mouse IgG	Thermo Fisher Scientific	Cat# A-31571; RRID: AB_162542
Alexa 647 anti-guinia pig IgG	Thermo Fisher Scientific	Cat# A-21450; RRID: AB_141882
Chemicals, peptides, and recombinant proteins		
Standard diet	Envigo	Cat# 2018S
Methionine Choline Deficient diet	Research Diets	Cat# A02082002BR
Methionine Choline Deficient Control diet	Research Diets	Cat# A02082003BY
Choline Deficient High Fat diet	Research Diets	Cat# A06071302
Western diet	Envigo	Cat# TD.88137
High Fat diet	Research Diets	Cat# D12492
2-Methyl-2-butanol	Sigma-Aldrich	Cat# 240486
2,2,2-Tribromoethanol	Sigma-Aldrich	Cat# T48402
Paraformaldehyde	Sigma-Aldrich	Cat# P6148
10XPBS	QUALITY BIOLOGICAL	Cat# 119-069-131
cOmplete™, Mini, EDTA-free Protease Inhibitor Cocktail	Roche	Cat# 11836170001
Bio-Rad Protein Assay Dye Reagent Concentrate	Bio-Rad	Cat# 5000006
Immobilon-FL PVDF Membrane	Millipore	Cat# IPFL00010

(*Continued on next page*)

Continued

REAGENT or RESOURCE	SOURCE	IDENTIFIER
Tissue-Tek® O.C.T. Compound	Sakura Finetech	Cat# 4583
RIPA Buffer (10X)	Cell Signaling Technology	Cat# 9806
Sodium succinate dibasic hexahydrate	Sigma-Aldrich	Cat# S2378
Sodium azide	Sigma-Aldrich	Cat# S2002
Potassium Phosphate Monobasic, Crystal	J.T.Baker	Cat# 3246-05
Sodium Phosphate Dibasic, Anhydrous	J.T.Baker	Cat# 3828-05
Nitro Blue Tetrazorium	Sigma-Aldrich	Cat# 5514
Phenazine methosulfate	Sigma-Aldrich	Cat# P9625
Bovine catalase	Sigma-Aldrich	Cat# C9322
DAB tetrahydrochloride	AMRESCO	Cat# 430
Cytochrome c	Sigma-Aldrich	Cat# C2506
Calcium chloride	Sigma-Aldrich	Cat# C3881
Ethyl Alcohol 200 Proof	PHARMCO	Cat# 111000200
Glutaraldehyde 25% solution	Electron Microscopy Sciences	Cat# 16220
Osmium tetroxide 4% aqueous solution	Electron Microscopy Sciences	Cat# 19190
Uranyl Acetate Dihydrate	TED PELLA	Cat# 19481
Embed 812 Resin	Electron Microscopy Sciences	Cat# 14900
Methyl-5-Norbornene-2,3-Dicarboxylic Anhydride	Electron Microscopy Sciences	Cat# 19000
Dodecenyl Succinic Anhydride	Electron Microscopy Sciences	Cat# 13710
DMP-30	Electron Microscopy Sciences	Cat# 13600
Critical commercial assays		
ALT Activity Assay	Sigma-Aldrich	Cat# MAK052
Triglyceride Reagent	Thermo Scientific	Cat# TR22421
Cholesterol Reagent	Thermo Scientific	Cat# TR13421
Picro Sirius Red Stain Kit	Abcam	Cat# ab150681
Experimental models: Organisms/strains		
Mouse: WT: C57BL/6J	The Jackson Laboratory	# 000664
Mouse: *Ldlr*$^{-/-}$: B6.129S7-Ldlrtm1Her/J	The Jackson Laboratory	# 002207
Mouse: *Drp1*$^{flox/flox}$	Yamada et al. (2018)	N/A
Mouse: *Drp1*$^{flox/flox}$*::Parkin*$^{-/-}$	Yamada et al. (2018)	N/A
Mouse: *Drp1*$^{flox/flox}$*::p62*$^{-/-}$	Yamada et al. (2018)	N/A
Mouse: *Drp1*$^{flox/flox}$*::PINK1*$^{-/-}$	Yamada et al. (2019)	N/A
Oligonucleotides		
Non-targeting ASOs: 5′-GGCCAATACGCCGTCA-3′	Ionis Pharmaceuticals	N/A
OPA1-targeted ASOs #1: 5′-GTTTTAAAGTAGGTGG-3′	Ionis Pharmaceuticals	N/A
OPA1-targeted ASOs #2: 5′-ATGATATATCGAAGTT-3′	Ionis Pharmaceuticals	N/A
qRT-PCR primers for IL1b	Hernandez-Alvarez et al., 2019	N/A
qRT-PCR primers for TNFα	Hernandez-Alvarez et al., 2019	N/A
qRT-PCR primers for TGFβ	Hernandez-Alvarez et al., 2019	N/A
qRT-PCR primers for Collagen A1	Hernandez-Alvarez et al., 2019	N/A

(*Continued on next page*)

Continued

REAGENT or RESOURCE	SOURCE	IDENTIFIER
qRT-PCR primers for ACAT2	Hernandez-Alvarez et al., 2019	N/A
qRT-PCR primers for SCD1	Rinella et al., 2008	N/A
qRT-PCR primers for ACLY	This paper	NCBI: NM_134037.3
qRT-PCR primers for SREBP-1a	This paper	NCBI: NM_011480.4
qRT-PCR primers for SREBP-1c	Rinella et al., 2008	N/A
qRT-PCR primers for ACC1	This paper	NCBI: NM_133360.2
qRT-PCR primers for GPAT1	This paper	NCBI: NM_008149.4
qRT-PCR primers for FAS	Rinella et al., 2008	N/A
qRT-PCR primers for ACOT2	This paper	NCBI: NM_134188.3
qRT-PCR primers for ACOT1	This paper	NCBI: NM_012006.2
qRT-PCR primers for FABP1	This paper	NCBI: NM_017399.5
qRT-PCR primers for CIDEB	This paper	NCBI: NM_009894.3
qRT-PCR primers for SEC23A	This paper	NCBI: NM_009147.2
qRT-PCR primers for APOB	This paper	NCBI: NM_009693.2
qRT-PCR primers for SAR1A	This paper	NCBI: NM_009120.3
qRT-PCR primers for SEC13	This paper	NCBI: NM_024206.4
qRT-PCR primers for FATP2	Rinella et al., 2008	N/A
qRT-PCR primers for FATP4	Rinella et al., 2008	N/A
qRT-PCR primers for CD36	This paper	NCBI: NM_001159558.1
qRT-PCR primers for EHHADH	This paper	NCBI: NM_023737.3
qRT-PCR primers for CPT1a	This paper	NCBI: NM_013495.2
qRT-PCR primers for CPT2	Rinella et al., 2008	N/A
qRT-PCR primers for ACADL	This paper	NCBI: NM_007381.4
qRT-PCR primers for ACADM	This paper	NCBI: NM_007382.5
qRT-PCR primers for HADHA	This paper	NCBI: NM_178878.3
qRT-PCR primers for PDK4	This paper	NCBI: NM_013743.2
qRT-PCR primers for CS	This paper	NCBI: NM_026444.4
qRT-PCR primers for ACO1	This paper	NCBI: NM_007386.2
qRT-PCR primers for IDH2	This paper	NCBI: NM_173011.2
qRT-PCR primers for OGDH	This paper	NCBI: NM_001252287.2
qRT-PCR primers for DLST	This paper	NCBI: NM_030225.4
qRT-PCR primers for DLD	This paper	NCBI: NM_007861.5
qRT-PCR primers for SUCLG1	This paper	NCBI: NM_019879.3
qRT-PCR primers for SUCLG2	This paper	NCBI: NM_011507.3
qRT-PCR primers for SDHA	This paper	NCBI: NM_023281.1
qRT-PCR primers for SDHC	This paper	NCBI: NM_025321.3
qRT-PCR primers for PPARα	This paper	NCBI: NM_011144.6
qRT-PCR primers for UCP2	This paper	NCBI: NM_011671.5
qRT-PCR primers for Albumin	Wakabayashi et al., 2010	Primer Bank ID 33859506a1
Software and algorithms		
Fiji	Fiji	https://fiji.sc/
Prism	GraphPad	https://www.graphpad.com/scientific-software/prism/

RESOURCE AVAILABILITY

Lead contact

Further information and requests for resources and reagents should be directed to and will be fulfilled by the Lead Contact, Hiromi Sesaki (hsesaki@jhmi.edu)

Materials availability

This study did not generate new unique reagents.

Data and code availability

- All data reported in this paper will be shared by the lead contact upon request.
- This paper does not report original code.
- Any additional information required to reanalyze the data reported in this paper is available from the lead contact upon request.

EXPERIMENTAL MODEL AND SUBJECT DETAILS

Animal models

All of the work with animals was conducted according to the guidelines established by the Johns Hopkins University Committee on Animal Care and Use. Five-week-old C57BL/6J WT mice (Stock# 000664) and *Ldlr*$^{-/-}$ mice (Stock# 002207) were purchased from Jackson Laboratory. One week later on arrival, WT and *Ldlr*$^{-/-}$ mice started to eat following the diets used for the study of pathological characterization: standard diet (2018S; Envigo), MCD and control diets (A02082002BR and A02082003BY; Research Diets), CDHF diet (A06071302; Research Diets), and Western (TD.88137; Envigo) diet. Non-targeting ASOs (5′-GGCCAA-TACGCCGTCA-3′) and two independent OPA1-targeted ASOs (#1: 5′-GTTTTAAAGTAGGTGG-3′; #2: 5′-ATGATATATCGAAGTT-3′) at the dose of 50 mg/kg bodyweight in PBS were injected intraperitoneally once per week for six weeks. To test the role of p62, Parkin, and PINK1 in mitochondrial ubiquitination, control, p62-KO, Parkin-KO, and PINK1-KO mice (Yamada et al., 2018, 2019) were fed MCD and control diets for 6 weeks.

METHOD DETAILS

ASOs

ASOs were synthesized and chemically modified with phosphorothioate in the backbone and consisted of the "3-10-3 Gapmer" design, whereby the three nucleotides at each terminus of an ASO are each modified with 2′-4′ constrained ethyl residues, flanking a central deoxynucleotide region at Ionis Pharmaceuticals (Carlsbad, CA, USA) (Seth et al., 2010). The specificity of ASOs was evaluated at Ionis by determining how many transcripts are predicted to bind when allowing for mismatches of 0 or 1, as well as mismatches of 2 with 14 contiguous bases. Based on previous studies, these ASOs are not expected to retain activity towards transcripts with more than two mismatches (Cioffi et al., 1997; Vickers et al., 2003; Zhang et al., 2000). More specifically, the non-targeting control ASO was specifically selected based on the prediction that it does not bind any transcripts in the mouse genome based on this *in silico* prediction of specificity. Both OPA1-targeted ASO#1 and #2 are predicted not to bind any transcripts other than OPA1 transcripts with mismatches of 0 but have off-targets with mismatches of 1 or 2 with 14 contiguous bases. Importantly, none of the predicted off-target transcripts for the two OPA1 ASOs used overlap. The non-targeting control ASO did not cause liver pathologies.

Histology and immunofluorescence

Mice were anesthetized by intraperitoneal injection of Avertin and fixed by cardiac perfusion of ice-cold 4% paraformaldehyde in PBS as previously described (Kageyama et al., 2014; Yamada et al., 2018). The livers were dissected out and further fixed in 4% paraformaldehyde in PBS for 2 hs at 4°C. For H&E staining, the samples were dehydrated and embedded in paraffin. Paraffin sections were cut, and H&E stained at Johns Hopkins School of Medicine Pathology Core. For cryosections, the fixed livers were further incubated in PBS containing 30% sucrose overnight and frozen in OCT compound (4583; Sakura Fintek). Oil Red O staining of cryosections were performed at Johns Hopkins School of Medicine Pathology Core. To analyze fibrosis, frozen sections were stained with Picro Sirius Red Stain Kit (ab150681; Abcam) according to the manufacturer's instruction. For immunofluorescence microscopy, frozen sections of the livers were cut,

washed in PBS, and blocked in 10% sheep serum (Yamada et al., 2018, 2019). The sections were then incubated with primary antibodies followed by fluorescently-labeled secondary antibodies. H&E, Oil Red O and Sirius Red stained samples were observed using a microscope (model BX51; Olympus) equipped with a DP-70 color camera and 103 (0.3 NA) UIS2 objectives at Johns Hopkins University School of Medicine Microscope Facility. Samples for immunofluorescence microscopy were viewed using a Zeiss LSM800 GaAsP laser scanning confocal microscopes equipped with a 63X objective at Johns Hopkins University School of Medicine Microscope Facility as reported previously (Yamada et al., 2018, 2019). Image analysis was performed using Fiji ImageJ software.

Human NASH samples

Liver needle core biopsies of adult human patients with clinicopathologically confirmed non-alcoholic fatty liver disease were obtained from the files of the University of Colorado Department of Pathology, with appropriate institutional approval. The liver needle core biopsies were processed to formalin fixed paraffin embedded blocks per the typical clinical laboratory protocol and H&E and trichrome slides were prepared per the typical clinical laboratory protocol. An expert liver pathologist reviewed the slides to confirm the diagnosis of non-alcoholic fatty liver disease. Each biopsy was assigned a non-alcoholic fatty liver disease activity score and fibrosis stage per the system developed by the Non-alcoholic Steatohepatitis Clinical Research Network (Kleiner et al., 2005).

Western blotting

Mouse livers were harvested, flash-frozen in liquid nitrogen, and homogenized in RIPA buffer (9806; Cell Signaling) containing complete mini protease inhibitor (11836170001; Roche). Lysates were centrifuged at 14,000 g for 10 min, and the supernatants were collected. Protein concentrations were determined by the Bradford method (5000006; Bio-Rad). Proteins were separated by sodium dodecyl sulfate polyacrylamide gel electrophoresis (SDS-PAGE) and transferred onto Immobilon-FL (IPFL00010; Millipore). After blocking in 3% bovine serum albumin (BSA) in PBS/Tween-20 for 1 h at room temperature, the blots were incubated with primary antibodies. Immunocomplexes were visualized by appropriate secondary antibodies conjugated with fluorophores using a PharosFX Plus Molecular Imager (Bio-Rad) and Typhoon Molecular imager (Amersham). Band intensity was determined using Fiji ImageJ software.

Antibodies

Several primary antibodies were used: OPA1 (612607; BD Biosciences), PDH (ab110333; Abcam), GAPDH (MA5-15738; Thermo), HSP60 (12165; Cell Signaling), TOM20 (11802-1-AP; Proteintech), MPC1 (14462; Cell Signaling Technology), MPC2 (46141; Cell Signaling Technology), CS (14309; Cell Signaling Technology), ACO2 (6571; Cell Signaling Technology), DRP1 (611113; BD Biosciences), MFF (Gandre-Babbe and van der Bliek, 2008), IDH2 (56439; Cell Signaling Technology), Fumarase (4567; Cell Signaling Technology), SDHA (11998; Cell Signaling Technology), SDHB (ab14714; Abcam), SDHC (14575-1-AP; Proteintech), SDHD (6847; ProSci), ubiquitin (3933S; Cell Signaling Technology), and p62 (GP62-C; Progen). Secondary antibodies were purchased from Invitrogen: Alexa 488 anti-Rabbit IgG (A21206), Alexa 488 anti-Mouse IgG (A21202), Alexa 568 anti-mouse IgG (A10037), and Alexa 647 anti-mouse IgG (A31571).

ALT activity

To measure ALT activity, blood samples were collected from the tail of mice. ALT activity in the blood was determined by a coupled enzyme assay (MAK052; Sigma-Aldrich), which resulted in a colorimetric (570 nm) product proportional to the generated pyruvate, according to the manufacturer's protocol.

Histochemical measurements of electron transport chain complex activity

This assay was performed as previously described (Kageyama et al., 2012) with some modifications. Briefly, livers were dissected out and immersed in the OCT compound. OCT embedded samples were placed on a metal plate pre-cooled with liquid nitrogen until samples were completely frozen. Frozen livers were cut into 7 μm thick sections and mounted onto glass slides. For SDH activity, sections were incubated with 130 mM sodium succinate and 1.5 mM nitro blue tetrazolium, 0.2 mM PMS, and 1.0 mM sodium azide in 0.1 M phosphate buffer adjusted at pH 7.0 at 37°C for 40 min. For COX activity, sections were incubated with 0.5 mg/mL diaminobenzidine tetrahydrochloride, 2 μg/mL catalase, and 4 mM cytochrome c in phosphate buffer adjusted at pH 7.0 at 37°C for 80 min. The enzymatic reaction was terminated by rinsing

with distilled water. Stained samples were mounted and viewed using an Olympus BX51 microscope equipped with a DP-70 color camera.

Electron microscopy

We anesthetized mice using Avertin and fixed by cardiac perfusion of 2% glutaraldehyde, 3 mM $CaCl_2$, and 0.1 M cacodylate buffer, pH 7.4 (Wakabayashi et al., 2009; Yamada et al., 2018). Livers were dissected, cut into small pieces, and further fixed for 1 h. After washing, samples were post-fixed in 2.7% OsO_4 and 167 mM cacodylate, pH 7.4 for 1 h on ice. After washing in water, samples were incubated in 2% uranyl acetate for 30 min. After dehydration using ethanol and propylene oxide, samples were embedded in EPON resin. Ultrathin sections were obtained using a Reichert-Jung ultracut E, stained with 2% uranyl acetate and lead citrate, and viewed using a transmission electron microscope (H-7600; Hitachi) at Johns Hopkins University School of Medicine Microscope Facility.

Blood lipid analysis

To analyze blood lipid levels, triglyceride and cholesterol levels were measured using triglyceride reagent (TR22421; Thermo Scientific) and total cholesterol reagent (TR13421; Thermo Scientific) according to the manufacturer's instructions.

Real-time qPCR

Total RNAs were purified from snap-frozen livers using a RNeasy Mini Kit (74106; Qiagen) and reverse-transcribed using a ReadyScript cDNA Synthesis Mix (RDRT; Sigma-Aldrich) (Yamada et al., 2018). PCR was performed using a CFX96 real-time PCR detection system (BioRad) and PowerUp SYBR Green Master Mix (A25741; Thermo Scientific). The DNA oligos are listed in Table S2.

QUANTIFICATION AND STATISTICAL ANALYSIS

All data were presented as mean ± SD. Statistical analysis was performed using student's t-test and one-way analysis of variance with post-hoc Dunnett's test with Prism (GraphPad). $p < 0.05$ was considered statistically significant.